https://doi.org/10.1016/j.jmst.2020.05.049
This is the Pre-Published Version.

The following publication Li, Y., Jia, X., Zhang, W., Zhang, Y., Xie, G., Qiu, Z., ... & Jiao, Z. (2021). Formation and crystallization behavior of Fe-based amorphous precursors with pre-existing α-Fe nanoparticles—Structure and magnetic properties of high-Cu-content Fe-Si-B-Cu-Nb nanocrystalline alloys. Journal of Materials Science & Technology, 65, 171-181 is available at https://doi.org/10.1016/j.jmst.2020.05.049

Formation and crystallization behavior of Fe-based amorphous precursors with pre-existing a-Fe nanoparticles-Structure and magnetic properties of high-Cu-content Fe-Si-B-Cu-Nb

Yanhui Li[a], Xingjie Jia[a], Wei Zhang[a,*], Yan Zhang[b], Guoqiang Xie[c], Zhiyong Qiu[a],Junhua Luan[d], Zengbao Jiao[e]

[a] *Key Laboratory of Materials Modification by Laser, Ion, and Electron Beams (Ministry of ducation), School of Materials Science and Engineering, Dalian University of Technology, Dalian 116024, China*

[b] *Institute for Materials Research, Tohoku University, Sendai 980-8577, Japan*

[c] *School of Materials Science and Engineering, Harbin Institute of Technology (Shenzhen), Shenzhen 518055, China*

[d] *Center for Advanced Structural Materials, Department of Materials Science and Engineering, City University of Hong Kong, Hong Kong, China*

[e] *Department of Mechanical Engineering, The Hong Kong Polytechnic University, Hong Kong, China*

Abstract

Structure, crystallization behavior, and magnetic properties of as-quenched and annealed $Fe_{81.3}Si_4B_{13}Cu_{1.7}$ (Cu1.7) alloy ribbons and effects of Nb alloying have been studied. Three-dimensional atom probe and transmission electron microscopy analyses reveal that high-number-density Cu-clusters and Pre-existing Nano-sized α-Fe Particles (PN-α-Fe) are coexistence in the melt-spun Cu1.7 amorphous matrix, and the PN-α-Fe form by manners of one-direction adjoining and enveloping the Cu-clusters. Two-step crystallization behavior associated with growth of the PN-α-Fe and subsequent nucleation and growth of newly-formed α-Fe is found in the primary crystallization stage of the Cu1.7 alloy. The number densities of the Cu-clusters and PN-α-Fe in melt-spun $Fe_{81.3-x}Si_4B_{13}Cu_{1.7}Nb_x$ alloys are gradually reduced with enriching of Nb, and a fully amorphous structure forms at 4 at.% Nb, although smaller Cu-clusters still exist. After annealing, 2 at.% Nb coarsens the average size ($D_{\alpha\text{-Fe}}$) of the a-Fe grains from 14.0 nm of the Nb-free alloy to 21.6nm, and 4 at.% Nb refines the $D_{\alpha\text{-Fe}}$ to 8.9nm. The mechanisms of the α-Fe nucleation and growth during quenching

© 2021. This manuscript version is made available under the CC-BY-NC-ND 4.0 license http://creativecommons.org/licenses/by-nc-nd/4.0/

and annealing for the alloys with large quantities of PN-a-Fe as well as after Nb alloying have been discussed, and an annealing-induced α-Fe growth mechanism in term of the barrier co-contributed by competitive growth among the PN-α-Fe and diffusion-suppression effect of Nb atoms has been proposed. A coercivity (H_c) $\propto$ $D_{\alpha\text{-}Fe}^3$ correlation has been found for the nanocrystalline alloys, and the permeability is inverse with the H_c.

Keywords: Fe-based nanocrystalline alloy Cu-cluster Pre-existing a-Fe nanoparticle rystallization behavior Soft magnetic property

1. Introduction

Fe-based nanocrystalline soft magnetic alloys are attractive core materials for high-frequency transformers, switch-mode power supplies, and stator/rotor in motors due to their high saturation magnetic flux density (B_s) and permeability (μ), low core loss (W) in high frequency, and near-zero magnetostriction[1–3]. Fe-Si-B-Nb-Cu alloys (FINEMET)[4], known as the first nanocrystalline soft magnetic materials discovered 30years ago, have achieved large-scale applications by virtue of their low W, high μ, and good manufacturability. Subsequently developed Fe-(Zr/Hf/Nb)-B (NANOPERM)[5] and (Fe, Co)-(Zr/Hf/Nb)-B-Cu (HITPERM) nanocrystalline alloys[6] exhibit enhanced B_s and Curie temperatures, which are promising for high-temperature applications. Around 10 years ago, Fe-(Si, B)-Cu[7] and Fe-Si-B-P-Cu (NANOMET)[8,9] nanocrystalline alloys were successively developed, and the B_s of which has been increased dramatically due to the absence of Nb and other early transition elements, favoring the miniaturization of electronic devices.

The excellent soft magnetic properties of the Fe-based nanocrystalline alloys are attributed to a reduction of effective magnetocrystalline anisotropy, which is benefited from their composite structure of a-Fe nanograins uniformly dispersing in the amorphous matrix[2]. The dual-phase nanostructure is usually obtained by annealing amorphous precursors. Promotion of the α-Fe nanograins precipitation but suppression of their over growth is crucial to achieve high B_s and avoid increases in coercivity (H_c) and W[10]. The nanostructure formation mechanism has been studied in numerous work. For a typical $Fe_{73.5}Si_{13.5}B_9Nb_3Cu_1$ alloy, extended X-ray absorption fine structure studies by Kim et al.[11] and Ayers et al.[12,13] suggested that Cu atoms form Cu-rich regions (clusters) with a near-fcc structure from the very early stage of the crystallization process. Three-dimensional atom probe analysis by Hono et al.[14–16] confirmed that Cu-clustering occurs prior to the primary crystallization, and the Cu-clusters serve as heterogeneous nucleation sites for the α-Fe phase. They pointed out that the α-Fe nanograins formed during annealing are by manner of direct contacting the Cu-clusters in one direction but not enveloping the Cu-clusters[15]. On the other hand, large-sized Nb is of importance to promote the formation of the amorphous phase during melt-spinning, and to refine the α-Fe nanograins after annealing by inhibiting the long-range diffusion of Fe atoms, leading to the fine nanostructure and good magnetic softness[15–18]. The similar behaviors of Cu-clustering and α-Fe nucleation by annealing also exist in the Fe-Si-B-Cu[7,19] and Fe-Si-B-P-Cu[9,11,20,21] nanocrystalline systems with only a slight shift from the Cu-clusters to Cu_3P-like clusters for the P-bearing alloys. However, it is difficult to inhibit the excessive growth of the α-Fe grains for the high-B_s Fe- (Si, B, P, C)-Cu alloys

due to the absence of Nb and other large-sized elements, and hence a very high heating rate and precise control of annealing temperature are required to achieve the fine nanostructure[22–26]. Breakthrough of the trade-off between the B_s and manufacturability of the nanocrystalline alloys is still a challenging issue.

Recently, we developed Fe-Si-B-Cu alloys containing high Cu content of ≥ 1.7 at.%[27]. Benefiting from the promoted α-Fe nucleation by high concentration of Cu, large quantities of Preexisting Nano-sized α-Fe Particles (denoted as *PN-α-Fe*) are present uniformly in the amorphous matrix of the melt-spun alloys. The competitive growth among the high-number-density (high-N_d) PN-a-Fe occurs immediately upon heating, which inhibits excessive growth of the α-Fe grains, resulting in a fine nanostructure and excellent soft magnetic properties even under a low-heating-rate annealing. Considering that the Cu and Fe atoms are frozen fast by rapid quenching, the nucleation and growth manner of the PN-α-Fe, i.e., the position of the PN-α-Fe in relation to the Cu-clusters might be different from that induced by annealing. The size of the PN-α-Fe is small, which might be more conducive to capture the initial nucleation feature in comparison with that during anneal- ing which difficult to control. In addition, the special melt-spun structure with the PN-α-Fe might give rise to unique crystallization behavior and annealed structure, which should be further clarified.

In this work, aiming to elucidate the nucleation and growth manners of the α-Fe phase during rapid quenching and annealing for the precursors with large quantities of PN-α-Fe, the meltspun structure, crystallization behavior, and annealed structure of a high-Cu-content $Fe_{81.3}Si_4B_{13}Cu_{1.7}$ (denoted as *Cu1.7*) alloy have been investigated.

Considering that Nb alloying might improve the amorphous-forming ability (AFA) and change the quantity of the PN-α-Fe in the melt-spun state, the synergistic effects of the PN-α-Fe and large-sized Nb on the nanocrystallization is worthy of discussion. Hence 1–4 at.% Nb has been alloyed into the Cu1.7 alloy, and the melt-spun and annealed structure along with thermal and magnetic properties have been studied. For comparison, the effects of Nb alloying into a benchmark $Fe_{81.7}Si_4B_{13}Cu_{1.3}$ (denoted as *Cu1.3*) alloy with a fully amorphous melt-spun structure have been investigated as well. The mechanism of the annealing-induced α-Fe growth has been proposed in term of the barrier co-determined by the competitive growth among the PN-α-Fe and diffusion-suppression effect of Nb atoms.

2. Experimental

Alloy ingots with nominal compositions of $Fe_{81.3-x}Si_4B_{13}Cu_{1.7}Nb_x$ (x = 0–4) and $Fe_{81.7-y}Si_4B_{13}Cu_{1.3}Nb_y$ (y = 0—4) in at.%, hereinafter denoted as $Cu_{1.7}Nb_x$ and $Cu_{1.3}Nb_y$, respectively, were prepared by arc melting a mixture of Fe, Si, B, Cu, and Nb elements with purities of ≥ 99.5 mass% under Ti-gettered argon atmosphere. Alloy ribbons with a width of 1.5mm and a thickness of 20μm were prepared by single-roller melt spinning with a surface linear velocity for copper wheel of 40m/s. The ribbons were sealed in vacuumed quartz tubes and subse- quently isothermally annealed at temperatures of 638–898K for 60min followed by water-quenching to prepare nanocrystalline samples. Heating rate to reach the set annealing temperature (T_a) is around 0.33K/s. Structure of the samples before and after annealing was examined by

X-ray diffraction (XRD, Bruker D8 Focus) with Cu Ka radiation and transmission electron microscopy (TEM, JEOL JEM-2010), respectively. Elemental distributions were investigated by three-dimension atom probe tomography (3D- APT). Needle-shaped specimens required for the 3D-APT were fabricated by lift-outs and annular milled in a FEI Scios focused ion beam/scanning electron microscope (FIB/SEM). The APT char- acterizations were performed in a local electrode atom probe (CAMEACA LEAP 5000 R). The specimens were analyzed at 50K in voltage mode, a pulse repetition rate of 200 kHz, a pulse fraction of 20%, and an evaporation detection rate of 0.5 % atom per pulse. Imago Visualization and Analysis Software (IVAS) version 3.8 was used for creating the 3D reconstructions and data analysis. Thermal properties were measured by differential scanning calorimetry (DSC, TA Q20) at a heating rate of 0.67K/s. To investigate the struc- ture evolution in the early crystallization stage, the ribbons were isochronally heated to specific temperatures at the heating rate of 0.67K/s by the DSC and immediately cooled. The B_s and H_c were measured by a vibrating sample magnetometer (VSM, Lakeshore 7404S) and a dc *B-H* loop tracer (Linkjoin MATS-2010SD) under maximum applied fields of 800 kA/m and 4000 A/m, respectively. The effective permeability (μ_e) in 1–100kHz were measured by a vector impedance analyzer (Agilent 4294A) under a field of 1A/m. The samples for the H_c and μ_e measurements were straight ribbons with a dimension of 70mm × 1.5mm ×20μm.

3. Results

3.1 Structure, crystallization behavior, and magnetic properties of Fe-Si-B-Cu alloys

3.1.1 Melt-spun structure

XRD patterns of the melt-spun Cu1.7 and Cu1.3 alloys both consist only of a series of broad maxima without any appreciably sharp diffraction peaks, indicating an amorphous feature (*see* Fig. S1 in Appendix A). However, the TEM results, as shown in Fig. 1, suggest different structure characteristics. For the Cu1.7 alloy, large quantities of particles in nanoscale can be found dispersing in the amorphous matrix from the bright-field TEM image (Fig. 1(a)). In the corresponding selected area electron diffraction (SAED) pat- tern, some spots matching (110) plane of the α-Fe can be observed embedding in the diffuse diffraction ring (inset in Fig. 1(a)). The high-resolution TEM (HRTEM) image (Fig. 1(b)) further confirms the coexistence of the amorphous matrix and α-Fe nanoparticles. The average grain size ($D_{\alpha\text{-Fe}}$) of the PN-α-Fe is 6.2 nm, and the number density ($N_{\text{d, }\alpha\text{-Fe}}$) is 2.2×10^{23} m^{-3} as estimated by $N_{\text{d, }\alpha\text{-Fe}} = N/(A\,D_{\alpha\text{-Fe}})$, where N is the quantity of the nanoparticles and A is the area of the TEM image. The inconsistency between the XRD and TEM results might be attributed to very small size and low volume fraction of the PN-α-Fe beyond the resolving power of the XRD[8,15]. For the Cu1.3 alloy, homogeneous bright-field TEM image, diffuse SAED halo, and maze-like HRTEM image (Fig. 1(c) and (d)) confirm the single amorphous phase without any detectable crystals.

Fig. 2(a) illustrates 3D-APT reconstruction maps of Fe, Si, B, and Cu elements of the melt-spun Cu1.3 alloy. The elements all exhibit homogeneous distributions without any chemical heterogeneity. For the Cu1.7 alloy, however, clear chemical segregation can be seen, especially of the Cu element (Fig. 2(b)). By highlighting the Cu element

with a 7at.% Cu iso-concentration surface (Fig. 2(c)), plenty of Cu-clusters with sizes of 2–4nm can be seen dispersing uniformly in the matrix. The average size ($D_{\text{Cu-cluster}}$) and number density ($N_{\text{d, Cu-cluster}}$) of the Cu-clusters are 2.9nm and $5.1 \times 10^{23}\,\text{m}^{-3}$, respectively. Fig. 2(d) presents the enlarged portion illustrating the Cu and Fe elements with 7 at.% Cu and 85 at.% Fe iso-concentration surfaces of the melt-spun Cu1.7 alloy. It is seen that the Fe nanoparticles, i.e., PN-α-Fe with sizes of 5–8nm are present immediately adjacent to the Cu-clusters in one direction (i.e., the Cu-cluster is at the interface of the α-Fe and amorphous phases) or by manner of enveloping the Cu-clusters taking the Cu-cluster as a core. Fig. 2(e) and (f) show elemental line scan spec- tra extracted from two selected cylindrical regions denoted as C_1 (φnm × 25 nm) and C_2 (φ1.5nm × 35nm) in the Fig. 2(d), respectively. The C_1 region successively goes across the amorphous matrix, Cu-cluster, PN-α-Fe, and amorphous matrix again, which can be revealed by the specific element concentration distribu- tions, respectively (Fig. 2(e)). The PN-α-Fe forms adjacent to the Cu-cluster. In the C_2 region, similar divisions of the Cu-cluster, α-Fe nanoparticle, and amorphous matrix can be found as well, whereas the position relation between the Cu-cluster and PN-α-Fe is different from the C_1. The PN-α-Fe forms surrounding the Cu-cluster core (Fig. 2(f)). The 3D-APT results provide a direct evidence for the two formation modes of the α-Fe phase during rapid quenching, i.e., by one-direction adjoining and enveloping the Cu-cluster. According to proximity histogram analysis, the average compositions of the amorphous matrix, Cu-cluster, and PN-a-Fe are $Fe_{80.7}Si_{5.3}B_{12.5}Cu_{1.5}$, $Fe_{13.1}Si_{3.0}B_{2.5}Cu_{81.4}$, and $Fe_{88.7}Si_{4.9}B_{4.9}Cu_{1.5}$, respectively. In comparison with the amorphous matrix, the Si

content in the PN-α-Fe changes slightly, whereas the B element is lean in the Cu-clusters and α-Fe due to the limit solubility. It should be mentioned that the Fe contents in the amorphous matrix and PN-α-Fe are very close, i.e., 80.7 at.% and 88.7 at.%, respectively, which are difficult to be distinguished in the total Fe atoms distribution shown in the Fig. 2(b).

3.1.2 Crystallization behavior and annealed structure of alloy with PN-α-Fe

Fig. 3(a) exhibits DSC curves of the melt-spun Cu1.7 and Cu1.3 alloys, and onset temperatures of the primary (T_{x1}) and second (T_{x2}) crystallizations are marked with black arrows in the figure, respectively. The T_{x1} of the Cu1.7 alloy is 634K, much lower than that (699K) of the Cu1.3 alloy, and the T_{x2} are both around 800 K. For the precursors of the soft magnetic nanocrystalline alloys, the T_{x1} is usually associated with the primary formation of the α-Fe and the T_{x2} corresponds to the non-ferromagnetic compounds. The lower T_{x1} of the Cu1.7 alloy indicates that a high content of Cu favors the precipitation of the α-Fe.

Two overlapped exothermic peaks are found in the early stage of the crystallization process of the $Cu_{1.7}$ alloy with large quantities of PN-α-Fe (Fig. 3(a)), which is quite different from the single sharp peak for the Cu1.3 and other common precursors with fully amorphous structure[4,6–8]. To understand this unique crystallization event, we investigated the structure evolution of the Cu1.7 alloy after isochronal annealing at temperatures corresponding to peak (665K) and offset (695K) temperatures of the earlier peak determined by Gaussian fitting, and offset temperature (750K) of the latter

peak, denoted as T_{a1}, T_{a2}, and T_{a3} in the Fig 3(a), respectively. Series of DSC curves of the annealed samples confirm the completion of the crystallization at respective T_a. The XRD and TEM results confirm that only the α-Fe phase forms after annealing. The bright-field image shows that the α-Fe grains in the sample after annealing at T_{a1} have a uniform size distribution with a $D_{\alpha\text{-Fe}}$ of 15nm (Fig. 3(b)). The $N_{d,\ \alpha\text{-Fe}}$ is $2.3 \times 10^{23} m^{-3}$, which is quite close to that of the PN-α-Fe in the melt-pun state. After annealing at T_{a2}, in addition to the grown PN-α-Fe maintaining their sizes at T_{a1}, there are plenty of newly-formed α-Fe grains with smaller sizes, and the $N_{d,\ \alpha\text{-Fe}}$ increases to $2.8 \times 10^{23} m^{-3}$ (Fig. 3(c)). After annealing at T_{a3}, the grain sizes become more uniform and the $N_{d,\ \alpha\text{-Fe}}$ shows no significant change (Fig. 3(d)). The results suggest that the former of the two overlapped peaks is associated with the growth of the PN-α-Fe (from ~6 to ~15nm), and the latter corresponds to the nucleation and growth of newly-formed α-Fe. For the Cu1.3 alloy, after isochronal annealing at T_{a1}' (710K) and T_{a2}' (750K), corresponding to the peak and offset temperatures of the first crystallization event, respectively, the $D_{\alpha\text{-Fe}}$ increases from 34 to 53nm, while the $N_{d,\ \alpha\text{-Fe}}$ keeps at around $4.4 \times 10^{21} m^{-3}$ (Fig. 3(e) and f). The increased $D_{\alpha\text{-Fe}}$ but nearly unchanged $N_{d,\ \alpha\text{-Fe}}$ reveals that the Cu1.3 alloy undergoes a successive α-Fe nucleation and growth during the primary crystallization, and the nucleation has almost accomplished at the first peak temperature.

The alloys were isothermally annealed at temperatures between T_{x1}−40K and T_{x2}−40K for 60min. We here focus on the structure of the alloys after annealing at an optimum temperature (T_{oa}), defined from the temperature at which the finest α-Fe nanostructure is obtained. After annealing at a T_{oa} of 668K, small α-Fe nanograins with

a $D_{\alpha\text{-Fe}}$ of 14nm can be found dispersing uniformly in the amorphous matrix of the Cu1.7 alloy, whereas the $D_{\alpha\text{-Fe}}$ for the Cu1.3 alloy is as large as 53.3nm (*see* Fig. S2 in Appendix A, latter Fig. 8(a) and (d)). The $N_{\text{d, }\alpha\text{-Fe}}$ for the annealed Cu1.7 alloy is around 2.8×10^{23} m^{-3}, which is nearly two orders higher than that (3.8×10^{21} m^{-3}) of the Cu1.3 alloy.

3.1.3 Magnetic properties

The Cu1.7 alloy after annealing at the T_{oa} possesses excellent soft magnetic properties, i.e., a low H_{c} of 7.1 A/m, high B_{s} of 1.77 T, and high μ_{e} of 16,500 and 14,800 at 1kHz and 100kHz, respectively. In comparison, the annealed Cu1.3 alloy has a higher H_{c} of 379.3A/m but lower B_{s} of 1.73 T and inferior μ_{e} of around 1370 at 1–100 kHz, respectively.

The effects of annealing heating rate (H_{r}) on the nanostructure and magnetic properties have been investigated as well (*see* Fig. S3 in Appendix A). As shown in Fig. 4, after annealing at 683K for 10min, the Cu1.7 alloy keeps the low H_{c} of around 7A/m at H_{r} of 50–400K/min. For the Cu1.3 alloy, the H_{c} is 99A/m at a H_{r} of 50K/min, and decreases gradually with increasing H_{r}, lowering to 24A/m at H_{r} of 400K/min. The B_{s} of the two alloys exhibits no significant change at H_{r} of 50–400K/min, i.e., 1.79–1.81T and 1.76–1.78T for the Cu1.7 and Cu1.3 alloys, respectively.

3.2 Effects of Nb alloying on structure and properties

3.2.1 Melt-spun structure

The XRD patterns of melt-spun $Cu_{1.7}Nb_x$ (x = 1–4) alloys all appear to be an amorphous feature without any crystalline peaks (Fig. S1). Similar to the Cu1.7 (x = 0) alloy, plenty of PN-α-Fe are present in the amorphous matrix of the x = 2 alloy, while the $D_{\alpha\text{-Fe}}$ and $N_{\text{d, }\alpha\text{-Fe}}$ get reduced to 4.3nm and 4.5×10^{22} m^{-3}, respectively (Fig. 5(a) and (b)). For x=4 alloy, no detectable α-Fe nanoparticles but homogeneous amorphous phase can be found in the bright-field TEM image (Fig. 5(c)). The HRTEM image showing the maze-like feature further confirms the fully amorphous structure (Fig. 5(d)). The TEM results demonstrate that the PN-α-Fe become less and smaller with enriching of Nb, and finally vanished at 4 at.%. For the Cu1.3 alloy, alloying of 1–4 at.% Nb maintains the amorphous feature in their melt-spun state (Fig. S1).

The elemental distributions of the melt-spun $Cu_{1.7}Nb_x$ alloys with x = 2 and 4 are shown in Fig. 6(a) and (b), respectively.The chemical segregation of the Cu can still be seen, while the heterogeneity degree gets decreased with the increase of Nb concentration. By measuring the 7 at.% Cu iso-concentration surface (Fig. 6(c) and (d)), the $D_{\text{Cu-cluster}}$ are 3.0 and 2.0nm, and the $N_{\text{d,Cu-cluster}}$ are 3.7×10^{23} and 2.7×10^{23} m^{-3} for the alloys with x = 2 and 4, respectively. By highlighting the 7 at% Cu and 85 at.% Fe iso-concentration surfaces, the PN-α-Fe with partial enveloping the Cu-clusters can be found for the x = 2 alloy (Fig. 6(c)). For the x = 4 alloy, no distinct α-Fe nanoparticle can be found although the Cu-clusters still exist in the amorphous matrix (Fig. 6(d) and (e)). This is also consistent with the TEM results (Fig. 5(d)). The proximity histogram analysis reveals that the average compositions of the Cu-clusters are $Fe_{18.8}Si_{4.2}B_{2.4}Cu_{73.3}Nb_{1.3}$ and $Fe_{46.6}Si_{5.6}B_{4.8}Cu_{41.2}Nb_{1.8}$ for the alloys with x = 2 and

4, respectively. The $D_{\text{Cu-cluster}}$, $N_{\text{d, Cu-cluster}}$, $D_{\text{a-Fe}}$ and $N_{\text{d, a-Fe}}$ of the melt-spun $Cu_{1.7}Nb_x$ (x = 0, 2, and 4) alloys are listed in Table 1.

3.2.2 Crystallization behavior and annealed structure

Fig. 7(a) shows DSC traces of the melt-spun $Cu_{1.7}Nb_x$ (x = 0–4) alloys. The T_{x1} and T_{x2} rise gradually with increase of the x value, indicating that Nb alloying improves the thermal stability of the as-quenched and residual amorphous phases. The temperature interval (*OT*) between the T_{x1} and T_{x2} is also widened (Table 2), which will benefit obtaining single α-Fe phase without other nonferromagnetic phase, facilitating to achieve good soft magnetic properties in a wider T_a range. Noting that two overlapped exothermic peaks can be found for the alloys with x = 0–2, and this characteristic becomes less obvious with increase of the x value and finally invisible when $x \geq 3$. The intensity of the former in the over- lapped peak gradually decreases while that of the latter enhances with increasing x from 0 to 2 (Fig. 7(a)), indicating that the volume fraction of the PN-α-Fe gets reduced with enriching of Nb. Since the melt-spun x = 4 alloy is fully amorphous, only one single crystallization peak associated with the new α-Fe formation is present. For the $Cu_{1.3}Nb_y$ (y = 0–4) alloy series, the T_{x1}, T_{x2}, and ΔT also get raised after Nb alloying (Fig. 7(b) and Table 2). The increased T_{x1}, T_{x2}, and broad crystallization exothermic peaks suggest that the Nb inhibits the precipitation of the crystalline phases.

Fig. 8(a)–(c) shows the bright-field TEM images along with the corresponding SAED patterns and grain size distributions of the $Cu_{1.7}Nb_x$ alloys after annealing at their

T_{oa}, i.e., 668,743,and 783K for x = 0, 2, and 4, respectively. The a-Fe phase precipitates for all alloys, whereas the nanostructure is different from each other. With increasing x value from 0 to 2, the $D_{\alpha\text{-Fe}}$ increases from 14.0 to 21.6 nm and the $N_{d,\ \alpha\text{-Fe}}$ reduces from 2.8×10^{23} to $5.2 \times 10^{22} m^{-3}$. When x = 4, the $D_{a\text{-Fe}}$ decreases to 8.9 nm and the $N_{d,\ \alpha\text{-Fe}}$ rises to $4.1 \times 10^{23} m^{-3}$. As suggested from the more concentrated $D_{\alpha\text{-Fe}}$ distribution (inset in Fig. 8(c)), the x = 4 alloy also shows improved uniformity of the nanostructure. Table 2 lists the $D_{\alpha\text{-Fe}}$ and $N_{d,\ \alpha\text{-Fe}}$ of the annealed alloys. The $D_{\alpha\text{-Fe}}$ denoted by asterisks were calculated from Scherrer formula using the full width at half maximum of the $(110)_{\alpha\text{-Fe}}$ diffraction peak in the XRD patterns (Fig. S2). Noting that alloying of 2 at.% Nb into the Cu1.7 alloy coarsens the annealed structure, although it can refine the PN-α-Fe in the melt-spun state. For the annealed $Cu_{1.3}Nb_y$ (y = 0–4) alloys, as shown in Fig. 8(d)–(f) and Table 2, the $D_{\alpha\text{-Fe}}$ gradually reduces from 53.3 to 39.8nm with increasing x from 0 to 2, and remarkably decreases to 8.7nm when y = 4. The $N_{d,\ \alpha\text{-Fe}}$ slightly increases from 3.8×10^{21} to $5.6 \times 10^{21} m^{-3}$ with increasing x from 0 to 2, and greatly rises to $3.9 \times 10^{23} m^{-3}$ when x = 4.

3.2.3 Magnetic properties

Fig. 9(a) presents the change of H_c for the $Cu_{1.7}Nb_x$ (x = 0–4) alloys after annealing at different temperature for 60min. The data of the melt-spun alloys are shown for comparison. The H_c of the x=0 alloy maintains at around 7A/m in a T_a range of 638–683K, and rises to 37A/m when the T_a is up to 723K. Similarly, the H_c of the other alloys all remain certain minimum values in their respective T_{oa} range and get increased at

higher T_a. The sharp increase of the H_c is due to the formation of non-magnetic phase. In the aspect of compositional dependence, the minimum H_c for the x = 0 alloy is 7.1A/m, and it increases to 17.0A/m when x = 2, and then greatly decreases to 1.9A/m when x = 4. The T_{oa} range for obtaining the low H_c is also widened after Nb alloying (Fig.9(a)), revealing an excellent tolerance for the T_a fluctuation. The B_s first rises steadily with increasing the T_a and then decreases sharply at the temperature where the H_c greatly increases. The optimum B_s gradually decreases from 1.73 to 1.41T with increasing x from 0 to 4. The μ_e is inverse with the change of H_c. The x = 4 alloy possesses μ_e of 25,000 and 18,000 at 1kHz and 100kHz, respectively, higher than those of the x = 0 alloy (16,500 @1kHz and 14,800 @100kHz). The μ_e of the x = 2 alloy is less than 4000 at 1–100kHz. For the $Cu_{1.3}Nb_y$ alloys, as shown in Fig.9(b), the minimum H_c gradually decreases from 371.1 to 90.4A/m with increasing y from 0 to 2, and greatly lowers to 12.1 and 2.4A/m when y = 3 and 4, respectively. The significant H_c reduction indicates that at least 3 at.% Nb is necessary for improving the magnetic softness of the $Cu_{1.3}Nb_y$ alloys. The T_{oa} region is also widened with enriching of Nb. The B_s gradually decreases from 1.73 to 1.41T with increasing y from 0 to 4. The μ_e of the y = 4 alloy is 18,000 at 1kHz and 10,000 at 100kHz, much higher than those of the y = 0 and 2 alloys (< 2000 at 1–100kHz). The detailed magnetic properties of the alloys are listed in Table 2.

4. Discussion

4.1 Formations of Cu-clusters and PN-α-Fe under rapid quenching

A fully amorphous structure is obtained for the melt-spun Cu1.3 alloy while high-

N_d Cu-clusters and PN-α-Fe are co-existence in the Cu1.7 alloy. The distinguishing melt-spun structure is considered to be attributed to the different Cu concentration. Due to the large positive heat of mixing (ΔH_{mix} = +13kJ/mol) between Cu-Fe atom pair[28], Cu atoms tend to segregate from Fe atoms and aggregate into the Cu-clusters during annealing[12,15,20]. If the Cu concentration is high enough, such as 1.7 at.% Cu for the present alloy, the high driving force for the Cu separation from the amorphous phase leads to forming a large number of Cu-clusters even in the melt- spun state (see Fig. 2(b) and (c)). Subsequently, large quantities of PN-α-Fe are promoted to precipitate by taking the Cu-clusters as heterogeneous nucleation sites.

The 3D-APT analysis (Fig. 2(d)–(f)) reveals that the PN-α-Fe form by two modes, i.e., one-direction adjoining the Cu-cluster or enveloping the Cu-cluster. It is believed that the Cu-cluster has a nearest neighbor structure similar to fcc-Cu[11–13]. Due to the well matching between the lattices of $(110)_{\alpha\text{-Fe}}$ and $(111)_{fcc\text{-}Cu}$, the α-Fe tends to nucleate on the $(111)_{fcc\text{-}Cu}$ plane during melt-spinning and continue to grow along the newly-formed α-Fe/amorphous interface until the Fe-atoms are frozen, resulting in the formation of PN-α-Fe next to the Cu-clusters, which is consistent with the model provided by Hono et al.[14–16]. Since the Cu-clusters formed during melt-spinning is small (2–4nm), the fcc-like structure for some Cu-clusters might be too imperfect to lose the structural anisotropy. In this condition, the α-Fe might nucleate and grow in contact with the Cu-cluster/amorphous interface along arbitrary direction by taking the Cu-cluster as a core to reduce the total interfacial energy, forming the PN-α-Fe enveloping the Cu-clusters. This is parallel to another model proposed by Ayers et

al.[12,29]. The PN-α-Fe can not grow excessively during melt-spinning. Noting that some of the PN-α-Fe are even unable to completely envelope the Cu-clusters (Fig. 2(d)) because the Fe atoms are rapidly frozen under rapid quenching, while it right cap- tures a clear image of the very early stage of the α-Fe nucleation. For the melt-spun Cu1.3 alloy, there is no detectable Cu aggregation (Fig. 2(a)), which might be due to that 1.3 at.% Cu is lower than critical content for forming clusters during melt-spinning. In this condition, no PN-a-Fe are present as well.

The $D_{\text{Cu-cluster}}$ and $N_{\text{d, Cu-cluster}}$ for the melt-spun $Cu_{1.7}Nb_x$ alloys decrease with enriching of Nb, which is attributed to the enhanced AFA. The Nb has an atomic radius of 0.143nm, larger than those of 0.124, 0.115, and 0.082nm for Fe, Si, and B, respectively[30]. The OH_{mix} between Nb-Fe, Nb-Si, and Nb-B atomic pairs are 16, 56, and 54kJ/mol, respectively[28]. Alloying of appropriate Nb provides enhanced atomic size mismatch and new chemical affinities between the atomic pairs, which might improve the local packing efficiency and restrain the long-range diffusion of the atoms, leading to improved AFA[31]. The driving force for the Cu-clustering gets reduced, and hence the $D_{\text{Cu-cluster}}$ and $N_{\text{d, Cu-cluster}}$ are low-ered. In addition, from the concentration depth profile (Fig. 6(e)), distinct pile-ups of Nb can be seen near the interfaces of the Cu-cluster/amorphous matrix, indicating that the Nb stop the growth of the Cu-clusters by inhibiting the Cu atoms diffusion. It has been reported that the Cu-clusters with size small to 2nm might can not serve as the nucleation sites for the α-Fe[32]. The decreased $D_{\text{Cu-cluster}}$ and $N_{\text{d, Cu-cluster}}$ cut down the valid heterogeneous nucleation sites, resulting in reduced $N_{\text{d, α-Fe}}$. Moreover, the large-sized Nb can also impede the Fe atoms diffusion,

leading to a decreased $D_{\alpha\text{-Fe}}$. Consequently, both the size and quantity of the PN-α-Fe get decreased with enriching of Nb and vanished in the $Cu_{1.7}Nb_4$ alloy (Table 1).

4.2 Mechanism of annealing-induced α-Fe growth related to PN-α-Fe and Nb alloying

As shown in Fig. 10(a), the $D_{\alpha\text{-Fe}}$ in the nanocrystalline alloy obtained by annealing the Cu1.7 precursor with large quantities of PN-α-Fe is much smaller than that of the Cu1.3. The $Cu_{1.7}Nb_2$ alloy possesses a larger $D_{\alpha\text{-Fe}}$ than those of the $Cu_{1.7}Nb_0$ and $Cu_{1.7}Nb_4$ alloys, while the $D_{\alpha\text{-Fe}}$ in the $Cu_{1.3}Nb_y$ alloys monotonically decreases with enriching of Nb. Here we propose a simple mechanism in term of the barriers inhibiting the α-Fe growth during the low-heating-rate annealing to explain the diverse annealed structure. For the Cu1.7 alloy, fine PN-α-Fe with the $N_{d,\,\alpha\text{-Fe}}$ of ~$10^{23}m^{-3}$ distribute uniformly in the amorphous matrix. Upon annealing, the high-N_d PN-α-Fe grow together. The strong competitive growth effect among the large quantities of PN-α-Fe causes a high level of barrier to the α-Fe growth. The $N_{d,\,\alpha\text{-Fe}}$ of PN-α-Fe gets decreased with enriching of Nb, hence the competitive growth effect upon annealing is weakened, leading to a reduction of the barrier. As schematized in Fig. 10(b), the $N_{d,\alpha\text{–Fe}}$ (black dash curve) and the barrier contributed by the PN-α-Fe (blue solid curve) roughly show downtrends with increasing Nb content and become near zero when the alloy is fully amorphous. Noting that the barrier might be below base line when the $N_{d,\,\alpha\text{-Fe}}$ is small to cer- tain level, because a handful of PN-α-Fe could promote the growth of the α-Fe by providing the nucleation sites. On the other hand, the annealing-induced a-Fe growth

in the Fe-Si-B-Cu-Nb system is governed by the Nb diffusion[14–17]. The large size and strong chemical affinities between Nb and other constituents lead to a slow diffusion of the Nb atoms, which become obstacles suppressing the long-range diffusions of the Fe atoms during annealing. This can be revealed from the increased T_{x1} and widened exothermic peaks after Nb alloying (Fig. 7). As shown in the Fig. 10(b), the barrier contributed by the diffusion-suppression effect of Nb atoms (magenta solid curve) dramatically enhances with enriching of Nb. The total barrier to the α-Fe growth during annealing, as schema-tized by a red solid curve in the Fig. 10(b), is the sum provided by the PN-α-Fe and Nb with ignoring the other uncared factors in this work. It is seen that the total barrier shows a U-like shape with higher values at two terminals where represent the precursors with large quantities of PN-α-Fe (such as $Cu_{1.7}Nb_0$) and enough high concentration of Nb (such as $Cu_{1.7}Nb_4$), respectively. Consequently, more fine nanostructure can be obtained for the annealed alloys with x = 0 or 4 due to the larger total barrier, whereas the x = 2 alloy with a smaller barrier has more coarsening nanostructure (Fig. 10(a)). Noting that although some α-Fe nuclei also present in the melt-spun $Fe_{85}Si_2B_8P_4Cu_1$ alloy[22], the $N_{d,\ \alpha\text{-Fe}}$ ($\sim 3\times10^{21} m^{-3}$) is much smaller in comparison with the Cu1.7 alloy. The insufficient pre-existing α-Fe nuclei can not provide enough high barrier, leading to coarsened grains after the low-heating-rate annealing. For the $Cu_{1.3}Nb_y$ alloys with single amorphous phase in the meltspun state, the barrier is mainly contributed by Nb atoms, which increases with more Nb alloying. Hence the annealed structure gets refined gradually with enriching of Nb. It should be emphasized that although the $D_{\alpha\text{-Fe}}$ of the annealed $Cu_{1.7}Nb_2$ alloy is larger than the $Cu_{1.7}Nb_0$ and $Cu_{1.7}Nb_4$

alloys, it is much smaller than the $Cu_{1.3}Nb_2$ alloy (Fig. 10(a)). This might be benefited from the large number of Cu-clusters formed during annealing due to the high Cu content, which promote plenty of α-Fe nanoparticles nucleation and growth together, resulting in the competitive growth as well. Noting that the $D_{\alpha\text{-Fe}}$ of the annealed $Cu_{1.3}Nb_y$ alloys lowers dramatically when y≥3, and becomes close to that of the $Cu_{1.7}Nb_4$ alloy when y = 4, indicating that the diffusion-inhibition effect of the Nb atoms plays a major role when the Nb content is sufficiently high.

4.3 Correlation between structure and magnetic softness

As suggested from the Table 2, the H_c of the present nanocrys-talline alloys has a positive correlation to the $D_{\alpha\text{-Fe}}$. According to the random anisotropy model[2,33,34], the H_c of the Fe-based nanocrystalline soft magnetic alloys is proportional to $D_{\alpha\text{-Fe}}^6$ when $D_{\alpha\text{-Fe}}$ is below ~100nm. This correlation will transit to $H_c \propto D_{\alpha\text{-Fe}}^3$ in case of strong induced anisotropies exist, such as, when the uniaxial anisotropy (K_u) is approximately 2 times of the random magnetocrystalline anisotropy[35–38]. Fig. 11 shows the H_c *vs.* $D_{\alpha\text{-Fe}}$ of Fe-Si-B-Cu-(Nb) alloys in this work and Ref.[27]. A distinct linear correlation between the H_c and $D_{\alpha\text{-Fe}}^3$ can be found. The interstitial B atoms in the α-Fe nanograins are considered to be a possible origin of the large K_u, although the solubility of the B in the α-Fe is quite limited[35]. According to the 3D-APT analysis, the α-Fe phase contains around 5 at.% B due to the high overall B concentration up to 13 at.% in the present alloys, which might lead to a strong K_u. On the other hand, it has been reported that the complete release of the compressive stress in a melt-spun $Fe_{79}B_{16}Si_5$ ribbon surface requires annealing at 673K for 7h[39]. For the present samples annealed at 668–783K for

1h, the residual stress is believed to still exist, which would induce the large K_u. Both of the above two factors result in a $H_c \propto D_{\alpha\text{-Fe}}^3$ law. The variation of the μ with $D_{\alpha\text{-Fe}}$ of the nanocrystalline alloys obeys the correlation of $\mu \propto D_{\alpha\text{-Fe}}^{-6}$ according to the random anisotropy model[2]. When the K_u is dominant, the permeability behavior becomes complex. If the sample was magnetized parallel to the anisotropy axis, the μ is determined by domain wall pinning and hence inverse with the H_c as well[2].The present nanocrystalline alloys with lower H_c possess higher μ_e (Table 2), which might be consistent with the above situation. The reduced B_s of the Nb-containing nanocrys- talline alloys is attributed to that alloying of Nb by substitution of Fe results in a decreased amount of total magnetic moment by reducing the unfilled 3*d* orbit of the Fe atoms and a deterioration of the ferromagnetic exchange interaction by enlarging the distance between magnetic atoms[40].

5. Conclusions

In this work, we have clarified the PN-α-Fe formation man- ner and crystallization behavior of the melt-spun $Fe_{81.3}Si_4B_{13}Cu_{1.7}$ alloy and the effects of Nb alloying on the structure, thermal stabil- ity, and magnetic properties, and have discussed the mechanisms of the a-Fe nucleation and growth during quenching and annealing. The results are summarized as follows:

(1) The Cu-clusters with a $D_{\text{Cu-cluster}}$ of 2.9 nm and $N_{\text{d, Cu-cluster}}$ of $5.1 \times 10^{23} m^{-3}$ are present in the melt-spun Cu1.7 alloy, and the PN-a-Fe with a $D_{\alpha\text{-Fe}}$ of 6.2nm and $N_{\text{d},\alpha\text{-Fe}}$ of $2.2 \times 10^{23} m^{-3}$ also form by one-direction adjoining and enveloping the Cu-clusters.

The sizes and number densities of the Cu-clusters and PN-α-Fe in the melt-spun $Fe_{81.3-x}Si_4B_{13}Cu_{1.7}Nb_x$ alloys are gradually reduced with increasing Nb content. A fully amor- phous structure forms at 4 at.% Nb, although smaller Cu-clusters still exist.

(2) Two overlapped exothermic peaks are found in the primary crystallization stage for the alloys with the PN-α-Fe. The for- mer in the peaks is associated with the growth of the PN-α-Fe, and the latter corresponds to the subsequent nucleation and growth of newly-formed α-Fe phase.

(3) After annealing, the nanostructure with a $D_{\alpha\text{-Fe}}$ of 14.0nm is obtained for the Cu1.7 alloy, much finer than that of the Cu1.3 with a fully amorphous melt-spun structure. For the annealed $Fe_{81.3-x}Si_4B_{13}Cu_{1.7}Nb_x$ alloys, 2 at.% Nb coarsens the $D_{\alpha\text{-Fe}}$ to 21.6nm, and 4 at.% Nb refines the $D_{\alpha\text{-Fe}}$ to 8.9 nm. The $D_{\alpha\text{-Fe}}$ in the annealed $Fe_{81.7-y}Si_4B_{13}Cu_{1.3}Nb_y$ alloys gets decreased gradually from 53.3 to 8.7 nm with increasing Nb from 0 to 4 at.%.

(4) The strong competitive growth among the high-N_d PN-α-Fe and diffusion-suppression effect of the sufficient Nb play important roles in the nanostructure refinement by providing enough high level of barriers to the α-Fe growth during annealing. Weakening either of the effects might lead to structure coarsening. The corresponding annealing-induced α-Fe growth mechanism has been proposed.

(5) The H_c of the present Fe-based nanocrystalline alloys is linear proportional to $D_{\alpha\text{-Fe}}^3$, and the μ_e is inverse with the change of H_c.

Acknowledgements

The authors thank Xiangcheng Ren for conducting part of experiments. This work was financially supported by the National Natural Science Foundation of China (Nos.

51571047, 51771039, and 51871039); and the National Key Research and Development Program of China (No. 2017YFB0903903).

References

a. 1 M.E. McHenry, M.A. Willard, D.E. Laughlin, Prog. Mater. Sci. 44 (1999) 291–433.

[2] 2 G. Herzer, Acta Mater. 61 (2013) 718–734.

[3] 3 N. Denis, M. Inoue, K. Fujisaki, H. Itabashi, T. Yano,IEEE Trans. Magn. 53 (2017), 8110006.

[4] 4. Y. Yoshizawa, S. Oguma, K. Yamauchi, J. Appl. Phys. 64 (1988) 6044–6046.

[5] 5. K. Suzuki, A. Makino, A. Inoue, T. Masumoto, J. Appl. Phys. 74 (1993) 3316–3322.

[6] 6. M.A. Willard, M.Q. Huang, D.E. Laughlin, M.E. McHenry, J.O. Cross, V.G. Harris, C. Franchetti, J. Appl. Phys. 85 (1999) 4421–4423.

[7] 7. M. Ohta, Y. Yoshizawa, Jpn. J. Appl. Phys. 46 (2007) L477–L479.

[8] 8. A. Makino, H. Men, T. Kubota, K. Yubuta, A. Inoue, Mater. Trans. 50 (2009) 204–209.

[9] 9. A. Makino, T. Kubota, K. Yubuta, A. Inoue, H. Matsumoto, S. Yoshida,J. Appl. Phys. 109 (2011), 07A302.

[10] 10. P.B. Chen, T. Liu, F.Y. Kong, A.D. Wang, C.Y. Yue, G. Wang, C.T. Chang, X.M. Wang, J. Mater. Sci. Technol. 34 (2018) 793–798.

[11] 11. S.H. Kim, M. Matsuura, M. Sakurai, K. Suzuki, Jpn. J. Appl. Phys. 32 (1993) 676–678.

[12] 12. J.D. Ayers, V.G. Harris, J.A. Sprague, W.T. Elam, H.N. Jones, Acta Mater. 46 (1998) 1861–1874.

[13] 13. J.D. Ayers, V.G. Harris, J.A. Sprague, W.T. Elam, Appl. Phys. Lett. 64 (1994) 974–976.

[14] 14. K. Hono, A. Inoue, T. Sakurai, Appl. Phys. Lett. 58 (1991) 2180–2182.

[15] 15. K. Hono, D.H. Ping, M. Ohnuma, H. Onodera, Acta Mater. 47 (1999) 997–1006.

[16] 16 K. Hono, Prog. Mater. Sci. 47 (2002) 621–729.

[17] 17. M.E. McHenry, F. Johnson, H. Okumura, T. Ohkubo, V.R.V. Ramanan, D.E. Laughlin, Scripta Mater. 48 (2003) 881–887.

[18] 18. Y. Yoshizawa, Script Mater. 44 (2001) 1321–1325.

[19] 19. M. Ohta, Y. Yoshizawa, J. Phys,D: Appl. Phys. 44 (2011), 064004.

[20] 20 A. Makino, H. Men, K. Yubuta, T. Kubota, A. Inoue,J. Appl. Phys. 105 (2009), 07A308.

[21] 21. A. Makino, IEEE Trans. Magn. 48 (2012) 1331–1335.

[22] 22. P. Sharma, X. Zhang, Y. Zhang, A. Makino, Scripta Mater. 95 (2015) 3–6.

[23] 23. M. Ohta, Y. Yoshizawa, Appl. Phys. Express 2 (2009) 23005.

[24] 24. X.D. Fan, H. Men, A.B. Ma, B.L. Shen, J. Magn. Magn. Mater. 326 (2013) 22–27.

[25] 25. R. Xiang, S.X. Zhou, B.S. Dong, G.Q. Zhang, Z.Z. Li, Y.G. Wang, J. Mater. Sci. Mater. Electron. 25 (2014) 2979–2984.

[26] 26. L. Hou, X.D. Fan, Q.Q. Wang, W.M. Yang, B.L. Shen, J. Mater. Sci. Technol. 35 (2019) 1655–1661.
[27] 27. Y.H. Li, X.J. Jia, Y.Q. Xu, C.T. Chang, G.Q. Xie, W. Zhang, J. Alloy. Compd. 722 (2017) 859–863.
[28] 28. A. Takeuchi, A. Inoue, Mater. Trans. 46 (2005) 2817–2829.
[29] 29. J.D. Ayers, V.G. Harris, J.A. Sprague, W.T. Elam, H.N. Jones, Nanostruct. Mater. 9 (1997) 391–396.
[30] 30 O.N. Senkov, D.B. Miracle, Mater. Res. Bull. 36 (2001) 2183–2198.
[31] 31 W.H. Wang, Prog. Mater. Sci. 52 (2007) 540–595.
[32] 32. Y.M. Chen, T. Ohkubo, M. Ohta, Y. Yoshizawa, K. Hono, Acta Mater. 57 (2009) 4463–4472.
[33] 33 G. Herzer, IEEE Trans. Magn. 25 (1989) 3327–3329.
[34] 34 G. Herzer, IEEE Trans. Magn. 26 (1990) 1397–1402.
[35] 35. K. Suzuki, G. Herzer, Scripta Mater. 67 (2012) 548–553.
[36] 36 K. Suzuki, J.M. Cadogan, Phys. Rev. B 58 (1998) 2730–2739.
[37] 37. P. Sharma, X. Zhang, Y. Zhang, A. Makino,J. Appl. Phys. 115 (2014), 17A340.
[38] 38. K. Suzuki, N. Ito, J.S. Garitaonandia, J.D. Cashion, G. Herzer, J. Non-Cryst. Solids 354 (2008) 5089–5092.
[39] 39. M. Tejedor, J.A. Garcıc´a, J. Carrizo, L. Elbaile, J.D. Santos, J. Magn. Magn. Mater. 202 (1999) 485–891.
[40] 40. A.D. Wang, C.L. Zhao, A.N. He, H. Men, C.T. Chang, X.M. Wang, J. Alloy. Compd. 656 (2016) 729–734.

Figure captions

Fig. 1. (a) Bright-field TEM images inset with corresponding SAED patterns and grain size distribution with normal fitting, and HRTEM images of melt-spun $Fe_{81.3}Si_4B_{13}Cu_{1.7}$ (a, b) and $Fe_{81.7}Si_4B_{13}Cu_{1.3}$ (c, d) alloys.

Fig. 2. APT element maps of melt-spun $Fe_{81.7}Si_4B_{13}Cu_{1.3}$ (a) and $Fe_{81.3}Si_4B_{13}Cu_{1.7}$ (b) alloys; highlighting Cu with 7 at.% Cu iso-concentration surface (c), and enlarged portion illustrating Cu and Fe with 7 at% Cu and 85 at.% Fe iso-concentration surfaces (d) of $Fe_{81.3}Si_4B_{13}Cu_{1.7}$ alloy, and concentration depth profiles from selected cylindrical regions $c1$ (φ1.5 nm × 25nm) (e) and $c2$ ($1.5 nm × 35 nm) (f) shown in (d), respectively.

Fig. 3. DSC curves of melt-spun $Fe_{81.3}Si_4B_{13}Cu_{1.7}$ (Cu1.7) and $Fe_{81.7}Si_4B_{13}Cu_{1.3}$ (Cu1.3) alloys before and after isochronal annealing at different temperature (a) and the corresponding bright-field TEM images and grain size distributions with normal fitting. (b) Cu1.7, T_{a1} = 665 K; (c) Cu1.7, T_{a2} = 690 K; (d) Cu1.7, T_{a3} = 750 K; (e) Cu1.3, T_{a1}' = 710 K; (f) Cu1.3, T_{a2}' = 750 K.

Fig. 4. Variation in H_c of $Fe_{81.3}Si_4B_{13}Cu_{1.7}$ and $Fe_{81.7}Si_4B_{13}Cu_{1.3}$ alloys as a function of annealing heating rate.

Fig. 5. Bright-field TEM images inset with corresponding SAED patterns and grain size distribution with normal fitting, and HRTEM images of melt-spun $Fe_{81.3-x}Si_4B_{13}Cu_{1.7}Nb_x$ alloys. (a, b): x = 2; (c, d): x = 4.

Fig. 6. APT element maps of melt-spun $Fe_{81.3-x}Si_4B_{13}Cu_{1.7}Nb_x$ alloys with x = 2 (a) and x = 4 (b); highlighting Cu with 7 at.% Cu iso-concentration surface and enlarged portion illustrating Cu (and Fe) element(s) with 7 at% Cu (and 85 at.% Fe) iso-concentration

surface(s) of the alloys with x = 2 (c) and x = 4 (d), respectively, and (e) concentration depth profile from selected cylindrical region (φ5 nm × 25 nm) shown in (d).

Fig. 7. DSC curves of melt-spun (a) $Fe_{81.3-x}Si_4B_{13}Cu_{1.7}Nb_x$ and (b) $Fe_{81.7-y}Si_4B_{13}Cu_{1.3}Nb_y$ (x/y = 0–4) alloys.

Fig. 8. Bright-field TEM images inset with corresponding SAED patterns and grain size distributions with normal fitting of $Fe_{81.3-x}Si_4B_{13}Cu_{1.7}Nb_x$ and $Fe_{81.7-y}Si_4B_{13}Cu_{1.3}Nb_y$ alloys after annealing at T_{oa} for 60min. (a): x = 0, T_{oa} = 668 K; (b): x = 2, T_{oa} = 743 K; (c): x = 4, T_{oa} = 783 K; (d): y = 0, T_{oa} = 668 K; (e): y = 2, T_{oa} = 763 K; (f): y = 4, T_{oa} = 783 K.

Fig. 9. Variation in H_C of (a) $Fe_{81.3-x}Si_4B_{13}Cu_{1.7}Nb_x$ and (b) $Fe_{81.7-y}Si_4B_{13}Cu_{1.7}Nb_y$ (x/y = 0–4) alloys as a function of annealing temperature. The results in melt-spun state are shown for comparison.

Fig. 10. Variation in $D_{\alpha\text{-Fe}}$ of $Fe_{81.3-x}Si_4B_{13}Cu_{1.7}Nb_x$ and $Fe_{81.7-y}Si_4B_{13}Cu_{1.3}Nb_y$ (x/y = 0–4) nanocrystalline alloys as a function of Nb content (a), and schematic of barriers to annealing-induced α-Fe growth in $Cu_{1.7}Nb_x$ alloys with different melt-spun structure (b). Black dash curve schematizes $N_{d,\alpha\text{-Fe}}$ in melt-spun state.

Fig. 11. H_C *vs.* $D_{\alpha\text{-Fe}}$ for Fe-Si-B-Cu-(Nb) nanocrystalline alloys in this work and Ref.[27].

Fig 1

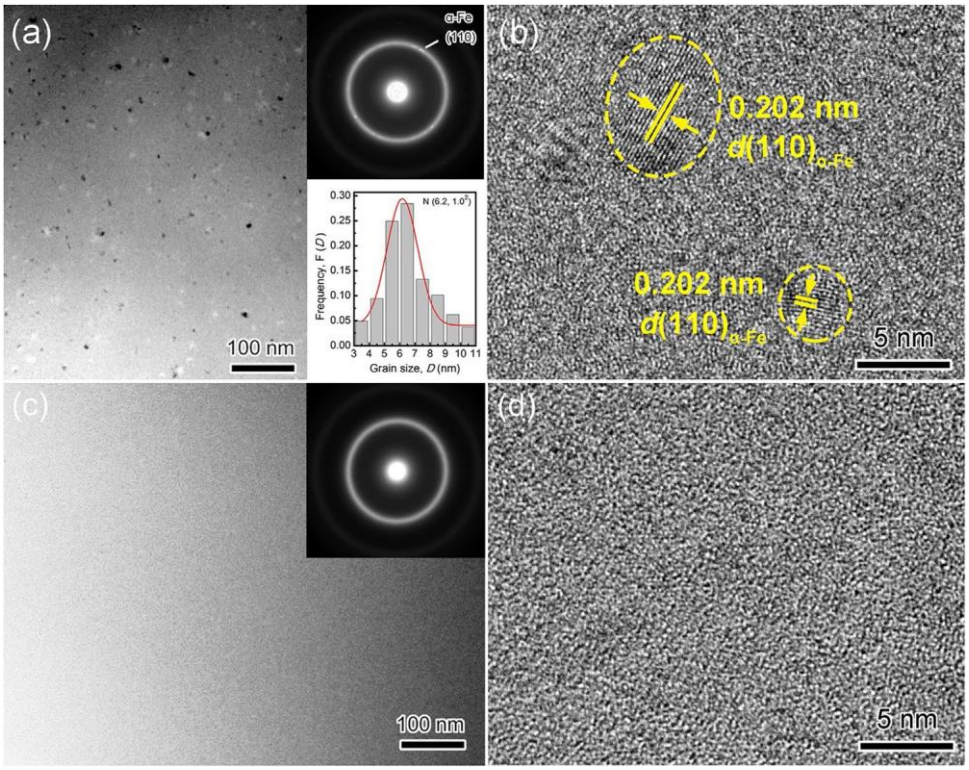
(a)
α-Fe
(110)
100 nm
N (6.2, 1.0²)
Frequency, F (D)
Grain size, D (nm)
(b)
0.202 nm
d(110)α-Fe
0.202 nm
d(110)α-Fe
5 nm
(c)
100 nm
(d)
5 nm

Fig 2

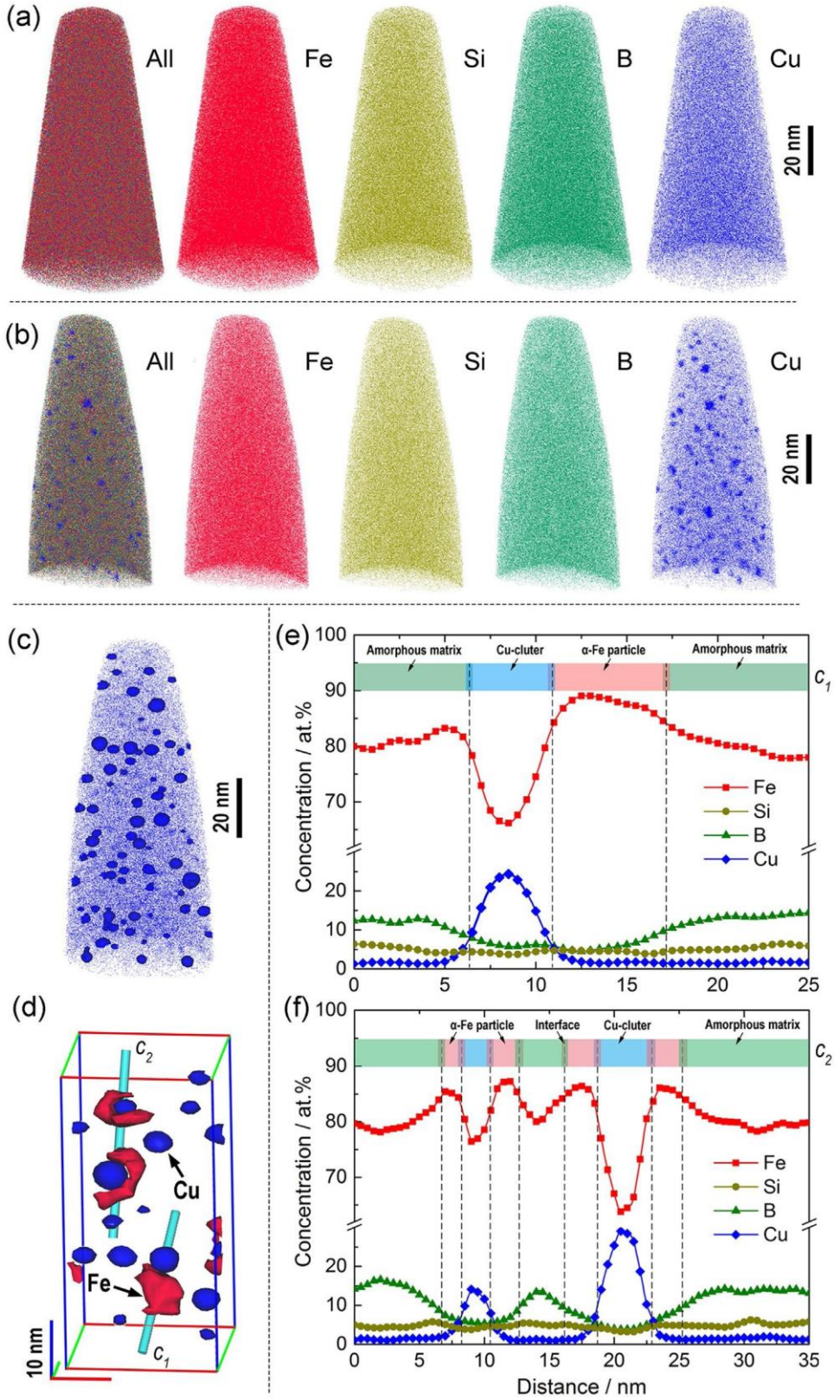
(a)
All
Fe
Si
B
Cu
20 nm
(b)
All
Fe
Si
B
Cu
20 nm
(c)
20 nm
(d)
C_2
Cu
Fe
C_1
10 nm
(e)
Amorphous matrix
Cu-cluter
α-Fe particle
Amorphous matrix
C_1
Concentration / at.%
Fe
Si
B
Cu
(f)
α-Fe particle
Interface
Cu-cluter
Amorphous matrix
C_2
Concentration / at.%
Fe
Si
B
Cu
Distance / nm

Fig 3

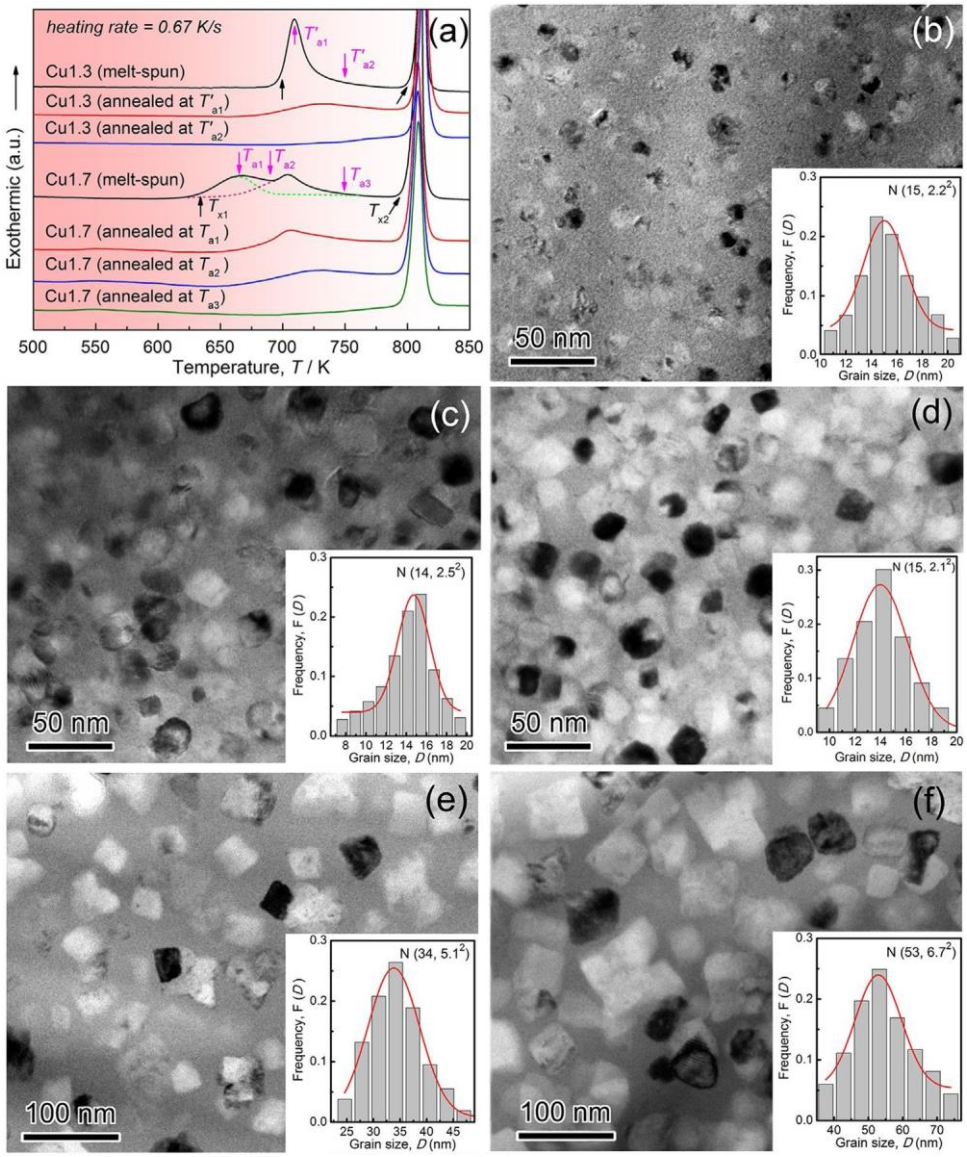
(a)
heating rate = 0.67 K/s
Cu1.3 (melt-spun)
Cu1.3 (annealed at T'a1)
Cu1.3 (annealed at T'a2)
Cu1.7 (melt-spun)
Cu1.7 (annealed at Ta1)
Cu1.7 (annealed at Ta2)
Cu1.7 (annealed at Ta3)
Exothermic (a.u.)
Temperature, T / K
(b)
50 nm
N (15, 2.2²)
(c)
50 nm
N (14, 2.5²)
(d)
50 nm
N (15, 2.1²)
(e)
100 nm
N (34, 5.1²)
(f)
100 nm
N (53, 6.7²)
Frequency, F (D)
Grain size, D (nm)

Fig 4

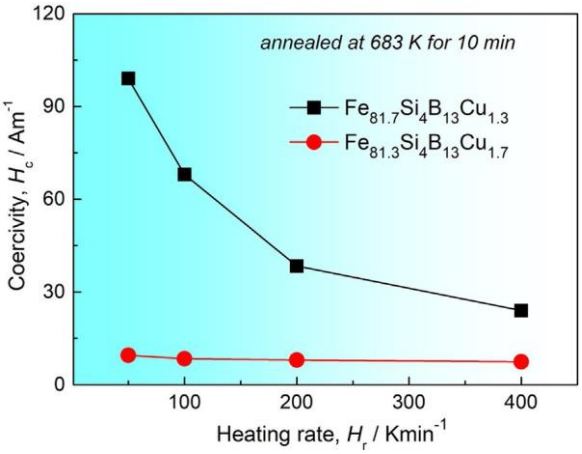
annealed at 683 K for 10 min
$Fe_{81.7}Si_4B_{13}Cu_{1.3}$
$Fe_{81.3}Si_4B_{13}Cu_{1.7}$
Coercivity, H_c / Am^{-1}
Heating rate, H_r / $Kmin^{-1}$
0
30
60
90
120
100
200
300
400

Fig 5

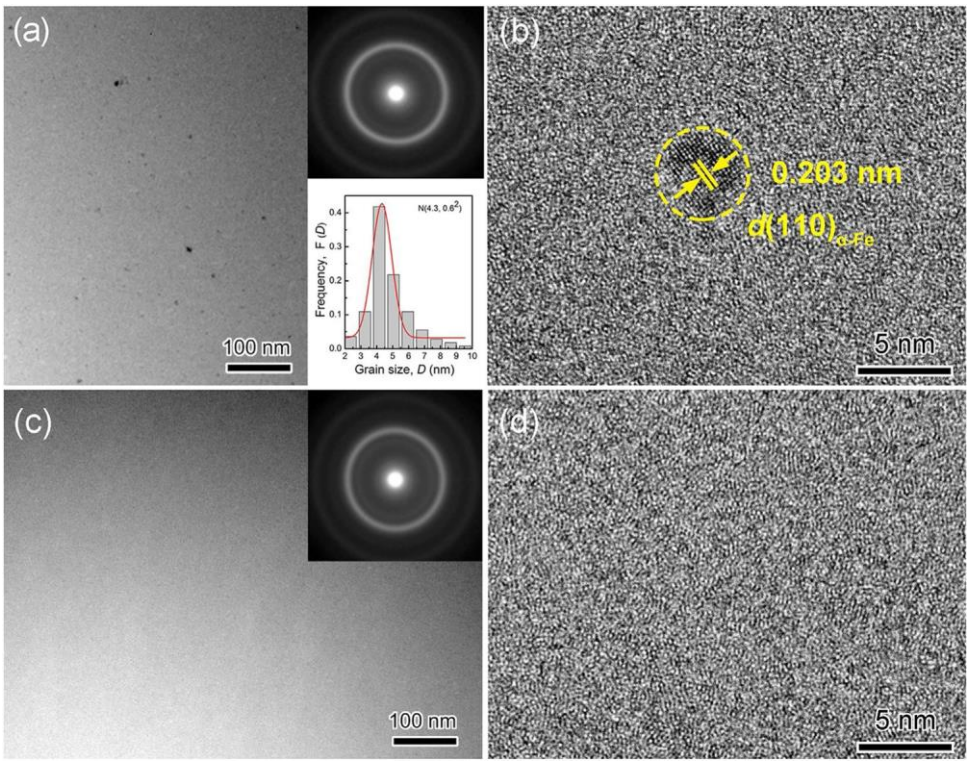
(a)
100 nm
N(4.3, 0.6^2)
Frequency, F (D)
Grain size, D (nm)
(b)
0.203 nm
d(110)α-Fe
5 nm
(c)
100 nm
(d)
5 nm

Fig 6

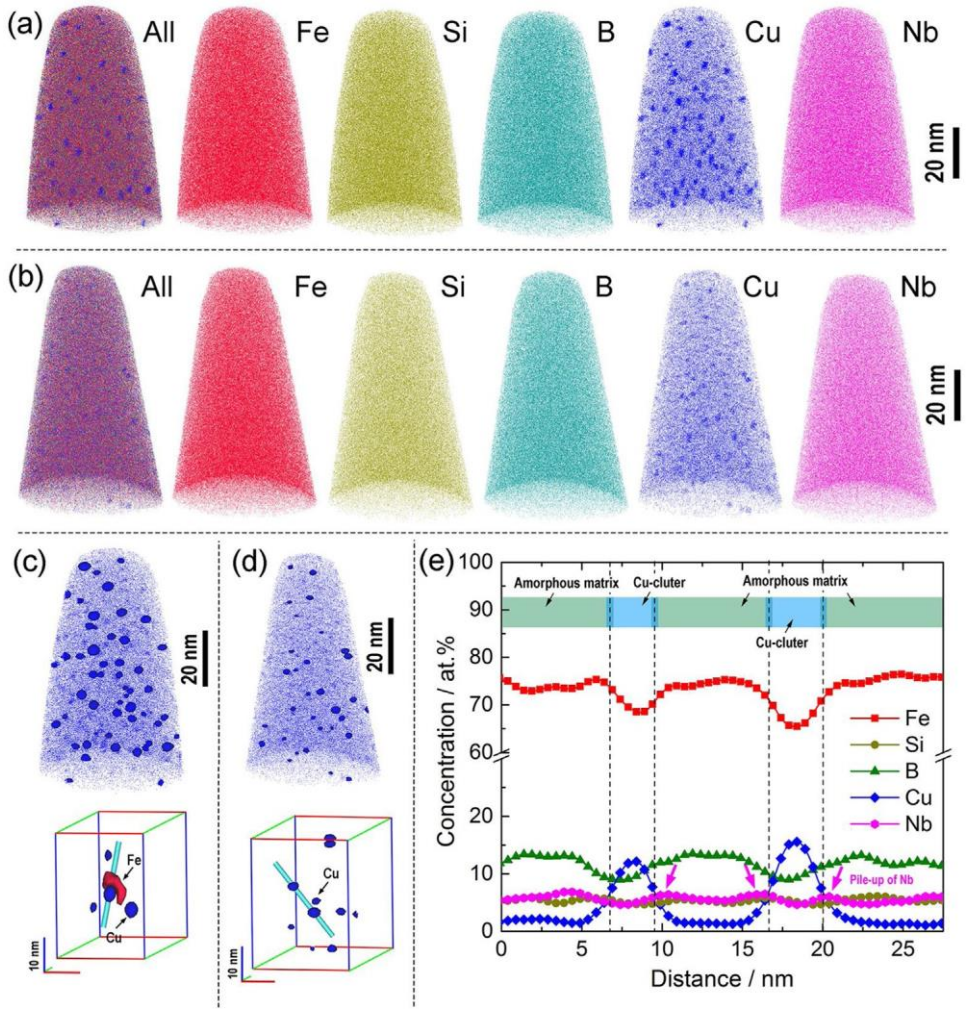
(a)
All
Fe
Si
B
Cu
Nb
20 nm
(b)
All
Fe
Si
B
Cu
Nb
20 nm
(c)
20 nm
Fe
Cu
10 nm
(d)
20 nm
Cu
10 nm
(e)
Amorphous matrix
Cu-cluter
Amorphous matrix
Cu-cluter
Concentration / at.%
Distance / nm
Fe
Si
B
Cu
Nb
Pile-up of Nb

Fig 7

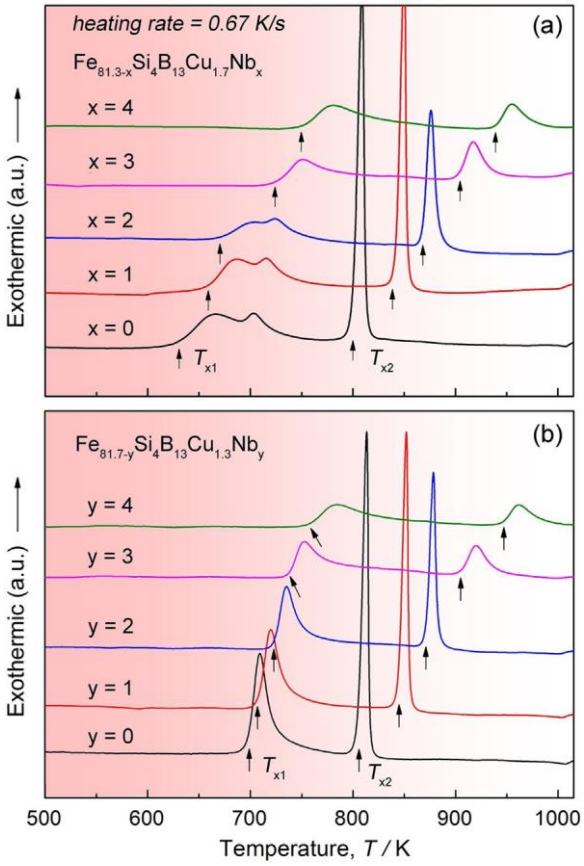
heating rate = 0.67 K/s
(a)
$Fe_{81.3-x}Si_4B_{13}Cu_{1.7}Nb_x$
x = 4
x = 3
x = 2
x = 1
x = 0
T_{x1}
T_{x2}
Exothermic (a.u.)
(b)
$Fe_{81.7-y}Si_4B_{13}Cu_{1.3}Nb_y$
y = 4
y = 3
y = 2
y = 1
y = 0
T_{x1}
T_{x2}
Exothermic (a.u.)
500
600
700
800
900
1000
Temperature, T / K

Fig 8

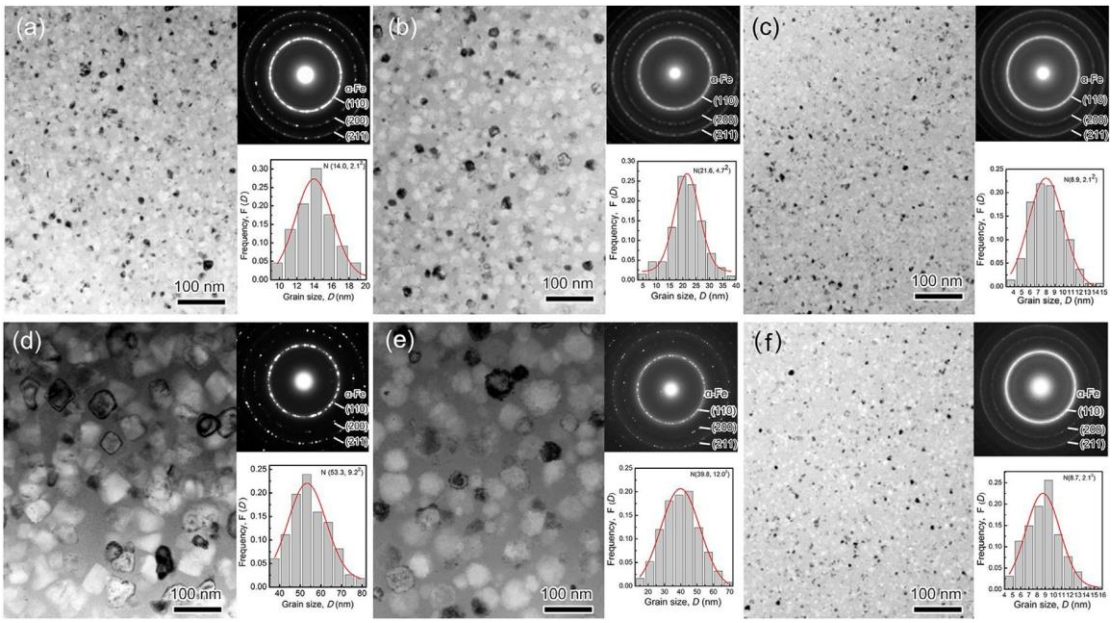

Fig 9

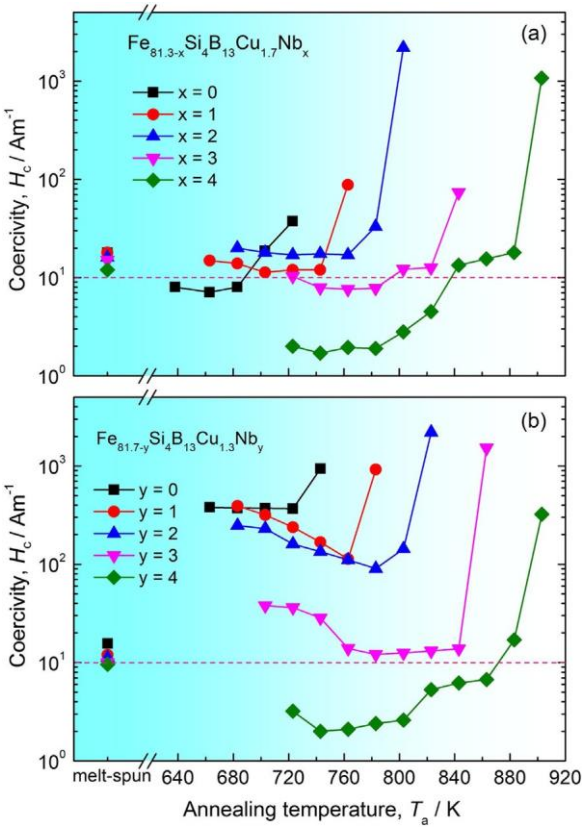
(a)
Fe81.3-xSi4B13Cu1.7Nbx
x = 0
x = 1
x = 2
x = 3
x = 4
Coercivity, Hc / Am-1
(b)
Fe81.7-ySi4B13Cu1.3Nby
y = 0
y = 1
y = 2
y = 3
y = 4
Coercivity, Hc / Am-1
melt-spun
640
680
720
760
800
840
880
920
Annealing temperature, Ta / K

Fig 10

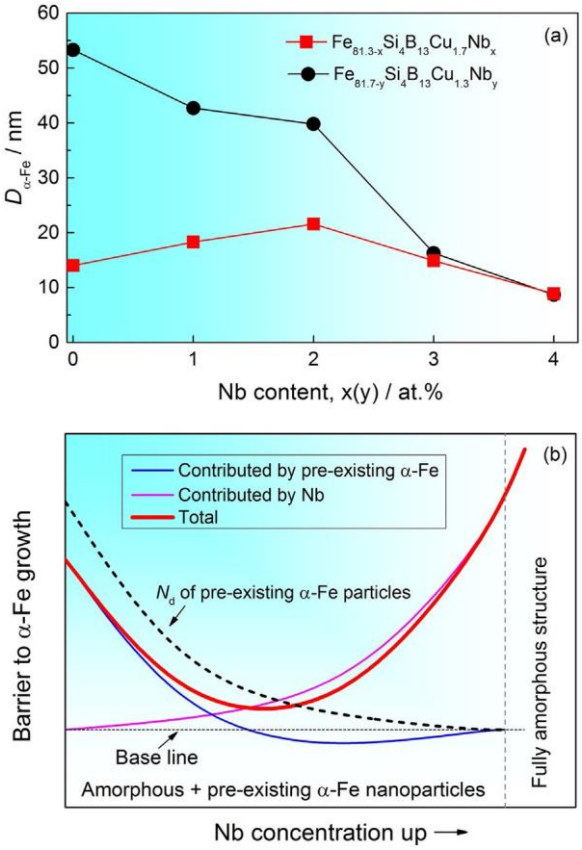
(a)
$Fe_{81.3-x}Si_4B_{13}Cu_{1.7}Nb_x$
$Fe_{81.7-y}Si_4B_{13}Cu_{1.3}Nb_y$
$D_{\alpha\text{-Fe}}$ / nm
Nb content, x(y) / at.%
(b)
Contributed by pre-existing α-Fe
Contributed by Nb
Total
N_d of pre-existing α-Fe particles
Base line
Amorphous + pre-existing α-Fe nanoparticles
Fully amorphous structure
Barrier to α-Fe growth
Nb concentration up

Fig 11

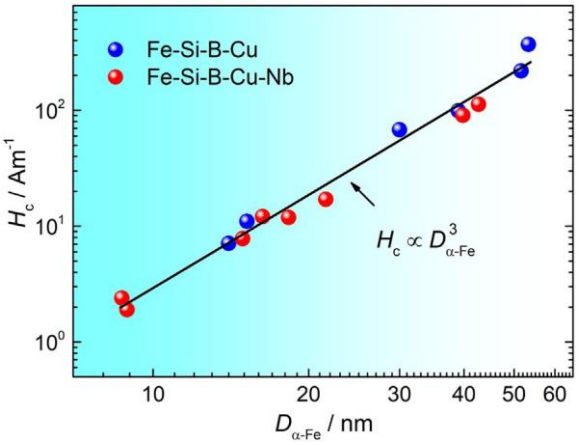
Fe-Si-B-Cu
Fe-Si-B-Cu-Nb
$H_c \propto D^3_{\alpha\text{-Fe}}$
H_c / Am^{-1}
10^0
10^1
10^2
10
20
30
40
50
60
$D_{\alpha\text{-Fe}}$ / nm